

# Mono-, Di-, and Tri-Valent Cation Doped $\text{BiFe}_{0.95}\text{Mn}_{0.05}\text{O}_3$ Nanoparticles: Ferroelectric Photocatalysts

Astita Dubey,\* Chin Hon Keat, Vladimir V. Shvartsman, Kirill V. Yusenko, Marianela Escobar Castillo, Ana Guilherme Buzanich, Ulrich Hagemann, Sergey A. Kovalenko, Julia Stähler, and Doru C. Lupascu

The ferroelectricity of multivalent codoped Bismuth ferrite ( $\text{BiFeO}_3$ ; BFO) nanoparticles (NPs) is revealed and utilized for photocatalysis, exploiting their narrow electronic bandgap. The photocatalytic activity of ferroelectric photocatalysts  $\text{BiFe}_{0.95}\text{Mn}_{0.05}\text{O}_3$  (BFM) NPs and mono-, di-, or tri-valent cations ( $\text{Ag}^+$ ,  $\text{Ca}^{2+}$ ,  $\text{Dy}^{3+}$ ; MDT) coinorporated BFM NPs are studied under ultrasonication and in acidic conditions. It is found that such doping enhances the photocatalytic activity of the ferroelectric NPs approximately three times. The correlation of the photocatalytic activity with structural, optical, and electrical properties of the doped NPs is established. The increase of spontaneous polarization by the mono- and tri-valent doping is one of the major factors in enhancing the photocatalytic performance along with other factors such as stronger light absorption in the visible range, low recombination rate of charge carriers, and larger surface area of NPs. A-site doping of BFO NPs by divalent elements suppresses the polarization, whereas trivalent ( $\text{Dy}^{3+}$ ) and monovalent ( $\text{Ag}^+$ ) cations provide an increase of polarization. The depolarization field in these single domain NPs acts as a driving force to mitigate recombination of the photoinduced charge carriers.


(RhB) when using polar  $\text{Ba}_{0.8}\text{Sr}_{0.2}\text{TiO}_3$  NPs as compared to nonpolar  $\text{Ba}_{0.2}\text{Sr}_{0.8}\text{TiO}_3$ .<sup>[4]</sup> Similarly, high photodegradation of methyl orange (MO) was reported when using  $\text{BiOIO}_3$  nanoplates, which was associated with local dipole moments of the  $\text{IO}_3$  pyramids, leading to strong macroscopic polarization.<sup>[5]</sup> A typical ferroelectric such as tetragonal  $\text{BaTiO}_3$  also shows increased photodegradation of RhB compared to paraelectric cubic  $\text{BaTiO}_3$ .<sup>[6]</sup> Zhang et al. showed that orthorhombic  $\text{KNbO}_3$  exhibits a higher photodegradation rate of RhB compared to monoclinic  $\text{KNbO}_3$  due to the larger polarity.<sup>[7]</sup> It has been argued that the internal electric field (depolarization field) inherent to FE materials assists the separation of photo-induced charge carriers and reduces their recombination rate.<sup>[8]</sup> The depolarization field originates from spontaneous polarization of FE, namely from the bound polarization charges. Typically, the depolarization

## 1. Introduction

Photoelectric properties of ferroelectrics (FE) have attracted interest of researchers working in the fields of photovoltaics,<sup>[1]</sup> photocatalysis (PC),<sup>[2]</sup> and photoelectrocatalysis.<sup>[3]</sup> It has been shown that the ferroelectric state is beneficial for PC performance. The positive effect of the FE state on PC was manifested in the increased photo-degradation rate of the dye rhodamine B

field is screened, at least partially, by free charge carriers either internal (electrons, holes, charged vacancies, or other point defects) or external (charged species from the environment or surface adsorbates). Nevertheless, even a partially screened depolarization field can be the main driving force for the photo-induced charge carrier separation in single domain FE photocatalysts, as it was observed for  $\text{PbTiO}_3$  nanoparticles.<sup>[9]</sup> The depolarization field can increase the charge carrier lifetime

A. Dubey, C. H. Keat, V. V. Shvartsman, M. E. Castillo, D. C. Lupascu  
Institute for Materials Science and Center for Nanointegration  
Duisburg-Essen (CENIDE)  
University of Duisburg-Essen  
Universitätsstr. 15, 45141 Essen, Germany  
E-mail: astita.dubey@uni-due.de

 The ORCID identification number(s) for the author(s) of this article can be found under <https://doi.org/10.1002/adfm.202207105>.

© 2022 The Authors. Advanced Functional Materials published by Wiley-VCH GmbH. This is an open access article under the terms of the Creative Commons Attribution-NonCommercial-NoDerivs License, which permits use and distribution in any medium, provided the original work is properly cited, the use is non-commercial and no modifications or adaptations are made.

K. V. Yusenko, A. G. Buzanich  
Federal Institute for Materials Research in Testing (BAM)  
Division Structure Analysis  
Richard-Willstätter-Str. 11, 12489 Berlin, Germany

U. Hagemann  
Interdisciplinary Center for Analytics on the Nanoscale (ICAN) and  
Center for Nanointegration Duisburg-Essen (CENIDE)  
University of Duisburg-Essen  
Lotharstr. 1-21, 47057 Duisburg, Germany

S. A. Kovalenko, J. Stähler  
Department of Chemistry  
Humboldt Universität zu Berlin  
Brook-Taylor-Str. 2, 12489 Berlin, Germany

DOI: 10.1002/adfm.202207105

(average amount of time that elapses between the generation and annihilation of excited carriers) via mitigating their recombination to ground state. So that these excited charge carriers diffuse and execute further chemical processes at the surface. Band bending at the surface of FE particles happens due to the effect of polarization in the proximity of the surface space charge region and it is considered as the main factor in the charge separation mechanism.<sup>[10,11]</sup> For positive domains (positive end of the polarization vector points toward the surface) downward band bending happens, whereas in negative domains (negative end of the polarization vector points toward the surface) polarization repels the electrons from the surface and hence upward band bending occurs. Moreover, when we increase the charge carrier density via photoexcitation, the width and height of the Schottky barriers changes, which modifies the interfacial band-bending.<sup>[12]</sup>

Although oxide FE are chemically robust, they usually have a large bandgap and a short charge carrier diffusion length, which limits their implementation in photoelectric applications. Therefore, significant attention has been given to narrowing the bandgap of oxide perovskites without compromise in their electronic and other unique functional properties to exploit the maximum amount of solar energy. There are several approaches, like defect engineering, heterojunction design, and metal oxide modifications to reduce the charge carrier recombination rate.<sup>[13]</sup>

Among the oxide ferroelectrics BiFeO<sub>3</sub> (BFO) is of particular interest due to its relatively narrow bandgap, ≈2.8 eV.<sup>[14]</sup> Moreover, this material has very large spontaneous polarization (75–80 μC cm<sup>-2</sup>).<sup>[15,16]</sup> The emergence of ferroelectricity in BFO is due to the stereochemically active 6s<sup>2</sup> lone pair of Bi<sup>3+</sup> that does not participate in the chemical bond and causes the Bi 6p (empty) orbital to come closer in energy to the O 2p orbitals, which allows their hybridization and consequently drives the off-centering of Bi<sup>3+</sup> with respect to the oxygen cuboctahedron that generates spontaneous polarization along the [111]<sub>c</sub> axis.<sup>[17]</sup> To enhance the polarization of BFO, researchers have introduced trivalent ions like Gd<sup>3+</sup>, Eu<sup>3+</sup>, La<sup>3+</sup>, Nd<sup>3+</sup>, or Sm<sup>3+</sup> into the Bi-site to improve the ferroelectric properties, arguing that smaller sized cations could cause unit cell distortions.<sup>[18]</sup>

Although the bandgap of bulk BFO is less than that of most oxide ferroelectrics, photons with energy less than 2.8 eV, which account for more than 80% of the solar spectrum, can still not be absorbed. This means that the quantum efficiency will inevitably be much lower than the ideal Shockley–Queisser limit. In addition, a similar loss in efficiency can be expected for PC of this material. As a solution, the bandgap can be reduced in nanosized BFO. For BFO NPs with size of 50 nm, a bandgap of ≈2.2 eV was reported.<sup>[19]</sup> Another way to change the bandgap is chemical modification. A large number of studies on the optical properties of BFO have been carried out by substituting Fe<sup>3+</sup>, since dopants at the Fe-site directly affect the electronic structure by participating in molecular orbital energy levels of FeO<sub>6</sub> octahedra.<sup>[20,21]</sup> Doping of Mn (up to 5 mol%) into the Fe-site not only enhances the light absorption of BFO NPs via contributions from *d–d* transitions,<sup>[22]</sup> while maintaining its ferroelectric polarization.<sup>[23,24]</sup> A large surface to volume ratio of material is needed for fast PC.<sup>[22]</sup> However, it has been reported that a reduction of particle size leads to a decrease in the ferroelectric

polarization of BFO.<sup>[25]</sup> To find a balance between the smaller size of NPs and large polarization, we have decided to substitute dopants into BFM NPs at the Bi-site. Namely, we compare between doping by monovalent (Ag<sup>+</sup>), divalent (Ca<sup>2+</sup>), and trivalent (Dy<sup>3+</sup>) ions at the Bi-site in BFM NPs based on their different ionic radii and different outermost atomic orbitals.

According to literature, Ca doping into BFO is effective for photodegradation of the Congo red dye and methylene blue.<sup>[26,27]</sup> It was reported that doping with Dy also enhances the photocatalytic activity of BFO NPs.<sup>[28,29]</sup> Ag doping in BFO NPs has not been studied so far. In our knowledge, FE properties in such doped NPs have not been studied.

The influence of heterovalent dopants at the Bi-site on the ferroelectric, optical and photocatalytic properties to our knowledge has not been studied extensively. In this work, we study the effect of mono-, di-, and trivalent doping on the photocatalytic activity of BFM NPs in relation to the doping induced variation of the optical properties, distortion of the crystal structure and nanoscale ferroelectricity.

## 2. Results

The sol–gel synthesized codoped NPs were structurally and optically characterized before their photocatalytic study. We use the following abbreviations in the manuscript; mono- (Ag<sup>+</sup>), di- (Ca<sup>2+</sup>), and tri- (Dy<sup>3+</sup>) valent cation doped: MDT; BiFeO<sub>3</sub>: BFO; BiFe<sub>0.95</sub>Mn<sub>0.05</sub>O<sub>3</sub>: BFM; Bi<sub>0.99</sub>Ag<sub>0.05</sub>Fe<sub>0.95</sub>Mn<sub>0.05</sub>O<sub>3</sub>: Ag-BFM; Bi<sub>0.95</sub>Ca<sub>0.05</sub>Fe<sub>0.95</sub>Mn<sub>0.05</sub>O<sub>3</sub>: Ca-BFM; Bi<sub>0.95</sub>Dy<sub>0.05</sub>Fe<sub>0.95</sub>Mn<sub>0.05</sub>O<sub>3</sub>: Dy-BFM. We also abbreviate a few terms used during photocatalysis, absence of ultrasonication; non-US, and presence of ultrasonication; US.

### 2.1. Crystal Structure and Morphology of NPs

Incorporation of Ag, Ca, and Dy, i.e., MDT onto the Bi-site of BFM NPs was successfully done using a modified sol–gel methodology as described in the Experimental Section. The structural, elemental, and morphological characterizations were done using X-ray diffraction (XRD) and transmission electron microscopy (TEM), high angle annular dark field imaging (HAADF), and energy dispersive X-ray (EDX). In **Figure 1**, the XRD results are shown. All NPs are single phase and exhibit R3c crystal structure (**Figure 1a,b**). The ionic radii of the doping elements play a vital role in the distortion of the crystal structure of pristine NPs. **Figure 1d** compares between ionic radii of the host and doping ions.<sup>[30]</sup> It can be seen that there is only a slight mismatch in the ionic radii between Fe and Mn, but a significant difference is found between the MDT and the Bi<sup>3+</sup> ions.

Heterovalent dopants can cause charge compensation to the system for overall electrochemical neutrality, either by altering the oxidation states of the B-site cations or by creating oxygen or A-site cation vacancies. To investigate the oxidation states of the host and doped elements in MDT NPs we measured surface sensitive X-ray photoelectron spectroscopy (XPS) as shown in **Figure S1** (Supporting Information). For undoped BFO and BFM NPs the oxidation states have been investigated by us before.<sup>[23]</sup>

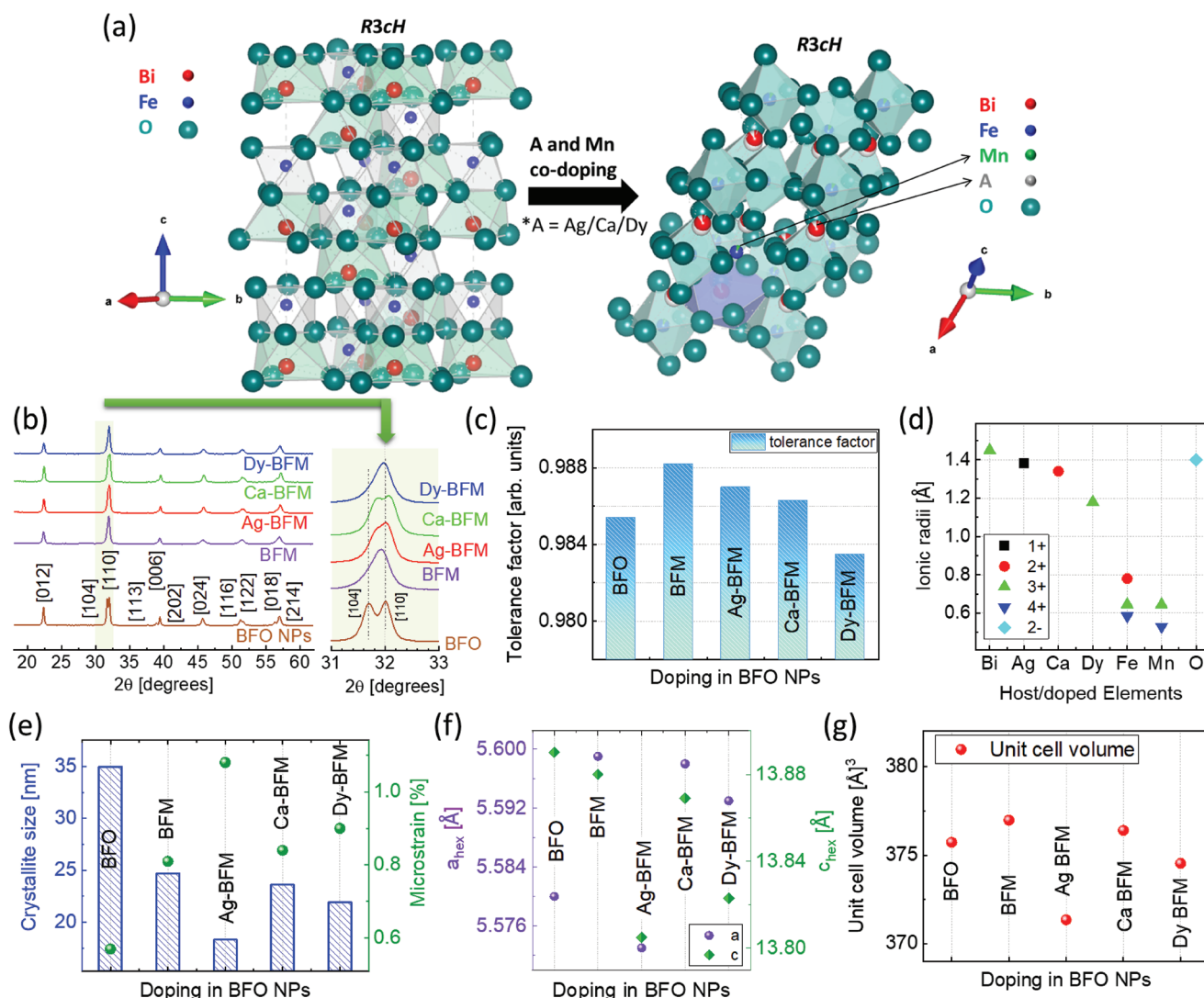


**Figure 1.** a) Doping at Bi and Fe site schematics, b) XRD diffractograms of doped NPs, c) tolerance factor trend, d) Ionic radii of host and doped elements, e) crystallite size and microstrain variation upon doping, f) altered lattice parameters due to doping, and g) unit cell volume variation. (Error bars are size of symbols).

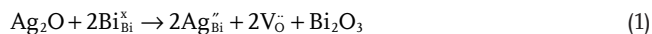
In the 4f XPS spectra of Bi, the 3+ state of the Bi ion is confirmed in all NPs. Similarly, the 2-oxidation state of oxygen is found in all NPs via 1s oxygen XPS spectra. In the 1s spectra of oxygen, the peaks at  $\approx 529$  and  $\approx 530$  eV correspond to lattice bound oxygen. The peaks at energies higher than 531 eV correspond to adsorbed  $-OH$  groups. Such peaks are more pronounced in Dy-BFM than Ag-BFM, which can be explained by the well-known lanthanide reactivity toward air and moisture.<sup>[31]</sup> In addition, carbonates and bicarbonates are also observed in the carbon XPS spectra of Dy-BFM.

The Fe-3p spectra of Dy-BFM, manifest the 3+ state of Fe. However, from the Fe-2p spectra of Ag-BFM, we found that the 3+ state is in majority over the 2+ state ( $7 \pm 5\%$ ) of Fe. The X-ray absorption near edge structure (XANES) spectra of the Fe K-edge also manifest the presence of Fe 3+ and 2+ states as shown in Figure 6. Dy is in its 3+ state as shown in the Dy 3d spectra. The 3d spectra of Ag show the 1+ oxidation state of it, with a slight shift of the peaks as compared to metallic

Ag. This slight shift is due to the bond strength of Ag in the crystal structure (Figure S1b, Supporting Information).<sup>[32]</sup> From the Mn-2p spectra, we obtain Mn 4+ as the main oxidation state with a slight amount of the 3+ state in Ag-BFM, however, for Dy-BFM we could only deconvolute the 3+ state of Mn. Nevertheless, from the XANES of Mn-K edge spectra, we found that only the 4+ state of Mn is present in all samples. The difference between the XPS and XANES results is related to their sensitivity to the surface and bulk states, respectively. So, we concluded that most of the Mn is in the 4+ state, but a small percentage of Mn is also present in the 3+ form at the surface of the NPs due to the termination of bonding chains at the surface which causes lower oxidation states of the ions.

Even if Mn is completely in the 4+ state, its concentration is not high enough to compensate the charge imbalance in Ag-BFM caused by the replacement of  $Bi^{3+}$  by  $Ag^+$ . The overall electric neutrality can be kept by formation of oxygen vacancies

as shown by the following defect equation in the Kroger–Vink notation (Equation (1))



For Ca-BFM, the 4+ state of Mn maintains charge balance, which has also been found for other divalent, i.e., Ba, doped BFM NPs.<sup>[23]</sup> For Dy-BFM NPs, the excessive positive charge due to the presence of Mn<sup>4+</sup> can be compensated via creation of cation vacancies. Both substitutional atoms and vacancies as a result of MDT doping could affect the crystal structure of NPs.

To study the potential crystal structure distortion, we first calculated the tolerance factor (*t*) for MDT-doped BFM NPs, based on the ionic radii as per their coordination numbers (Figure 1c). The incorporation of 5 mol% Mn at the Fe-site of BFO NPs increases the *t* value bringing it closer to the value of *t* = 1. Thus, the rhombohedral distortion of the BFO crystal structure diminishes due to Mn incorporation. However, upon MDT doping at the Bi-site in BFM NPs the tolerance factor decreases. For Dy-BFM the value of “*t*” is found to be smallest among all NPs and even smaller than pristine BFO NPs. The tolerance factor gives an estimate about the distortion in the crystal structure with respect to the ideal cubic structure, but the presence of anionic and cationic vacancies especially in Ag-BFM and Dy-BFM, respectively, can alter the crystal structure disparately.

At the same time, it can be seen that MDT doping into BFM NPs results in merging/demerging of XRD peaks at  $2\theta \approx 32^\circ$  [shaded region-Figure 1b]. To analyze this distortion in more detail, we performed a Rietveld refinement of the XRD-diffractograms, as shown in Figure S2 (Supporting Information). The fit characteristics are tabulated in Table S1 (Supporting Information), supporting the quality of the fits. According to the Rietveld refinement, all NPs exhibit rhombohedral (*R3c*) crystal symmetry without any secondary phase formation within the XRD detection limit. The lattice parameters, *a*, and *c* in the hexagonal representation, get altered upon MDT doping as shown in Figure 1f. The unit cell volume is smallest for Ag-BFM NPs and largest for Ca-BFM NPs among the MDT doped NPs as shown in Figure 1g. As compared to BFM NPs, Ca-BFM does not significantly alter the lattice parameters, but Dy-BFM does. In NPs, the resultant XRD peak broadening is due to a combine effect of reduced crystallite size and increased microstrain.<sup>[23,24]</sup> Crystallite size reduces upon MDT doping in BFM NPs (Figure 1e), where the smallest crystallite size and highest microstrain value are observed for Ag-BFM. Among the MDT-BFM NPs, Ca-BFM has the largest crystallite size. The XRD results reveal the presence of doping elements into the crystal structure and also unveil the distortion of the rhombohedral structure of BFM by mono-, di-, and tri-valent cation doping.

The overall distribution of doping elements in BFO NPs were confirmed by high-angle annular dark-field TEM measurements. The representative HAADF maps of elements in the Ag-BFM and Dy-BFM samples are shown in Figure 2 (right panels). It can be seen in the overlay images that all doped and host elements are homogeneously distributed. The stoichiometry of the host and doping elements are also confirmed by energy-dispersive X-ray spectroscopy (EDXS) (Table S2, Supporting Information). The shape, size, and morphology of the

NPs are investigated by high resolution TEM (Figure 2a–d). The average particle size of BFM and MDT-doped BFM NPs matches well with the average crystallite size obtained from the Rietveld refinement results (Figure 1e). The particle size is reduced upon MDT-doping as shown by histograms in the respective TEM images. Ag-BFM has the smallest particle size  $18 \pm 4$  nm, but there is no big difference in between the particle sizes of the MDT NPs. All doped NPs are single crystalline, but they have different shapes. BFM NPs are nearly spherical, whereas Ag-BFM NPs have elliptical morphology. For Ca-BFM NPs, similar elliptical morphology is found but with a distorted circumference. Interestingly, Dy-BFM NPs have an asymmetrical hexagonal shape different than the others as shown in their representative TEM images. These results unveil the role of dopants in the determination of shape and size of NPs, which is mainly influenced by the diffusion dynamics during the calcination step.

For NPs, the large surface to volume ratio is a crucial factor for their physical properties and related applications like photocatalysis. From BET data analysis, we found that Dy-BFM has the largest average surface area and pore volume among all MDT NPs, and Ag-BFM has the smallest among them, but still larger than BFM NPs (Figure S3, Supporting Information). The small surface area of Ag-BFM could be due to strong agglomeration of NPs.

## 2.2. Optical Properties of NPs

The optical properties of the NPs are determined using diffuse reflectance spectroscopy (DRS) and photoluminescence (PL) measurements. The measured reflectance spectra of all NPs are transformed into the corresponding absorption spectra (Figure 3a) by applying the Kubelka–Munk transformation (Equations (2) and (3))

$$F(R_\infty) = K/S = (1 - R_\infty)^2 / R_\infty \quad (2)$$

$$R_\infty = R_{\text{sample}} / R_{\text{reference}} \quad (3)$$

Where,  $F(R_\infty)$  is Kubelka–Munk function,  $R_\infty$  is the reflectance of the sample, and *K* and *S* are the absorption and scattering coefficients, respectively.<sup>[33]</sup> The BFO NPs manifest four absorption features at  $\approx 1.4$ , 1.9, 2.5, and 3.3 eV, as shown in our previous work.<sup>[22]</sup> The absorption maximum at 3.3 eV is attributed to the well-known *p* → *d* charge transfer transition in BFO, the main absorption edge at  $\approx 2.5$  eV corresponds to the bandgap transition of BFO, and the lower energy peaks at  $\approx 1.4$  and 1.9 eV are due to *d*–*d* transitions ( ${}^6\text{A}_{1g} \rightarrow {}^4\text{T}_{1g}$ , and  ${}^6\text{A}_{1g} \rightarrow {}^4\text{T}_{2g}$ ).<sup>[22]</sup> The BFM NPs show similar features as BFO, but with stronger absorption in the *d*–*d* transition region, which may be due to the distortion of energy levels caused by the Jahn–Teller cation (Mn<sup>3+</sup>).<sup>[22]</sup> When doping with MDT ions in BFM, we observe an increase in absorption not only in the *d*–*d* transition range, but also near  $\approx 2.5$  eV, which shows that the Bi-site substitution increases the total light absorption of the BFM NPs in the visible range from 3.5 to 1.3 eV. Among the MDT doped NPs, the Dy-BFM ones have the strongest absorption

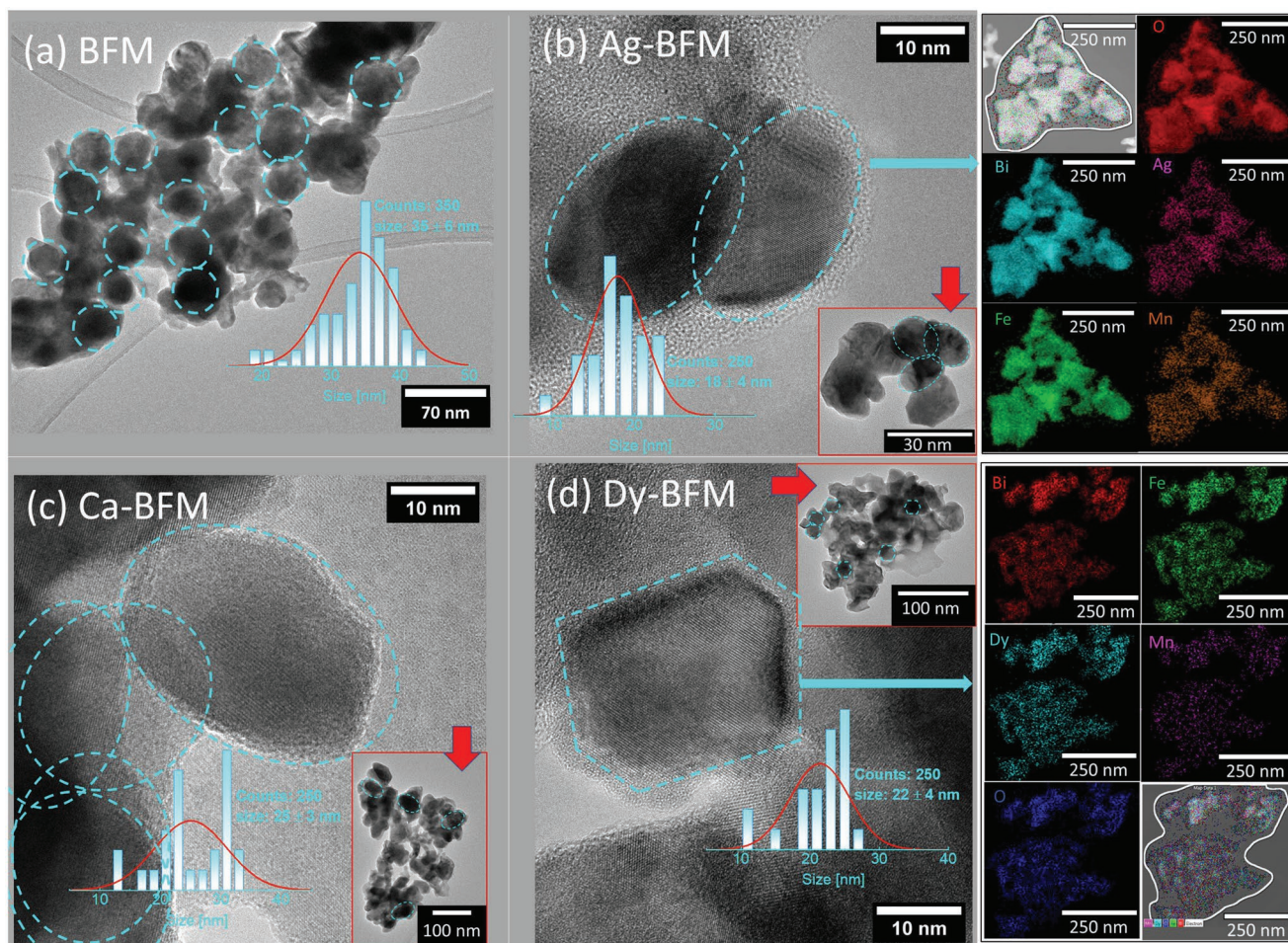


**Figure 2.** TEM images of MDT doped BFM NPs. in right side HAADF images of elements in Ag-BFM and Dy-BFM samples.

around 2.5 eV. The bandgap does not alter significantly upon doping, however, there are some transitions that will be analyzed in more detail. To study the effect of MDT doping on the bandgap transition the Tauc equation (Equation (4)) is used

$$(\alpha h\nu)^{1/\gamma} = B(h\nu - E_g) \quad (4)$$

where  $\alpha$  is the absorption coefficient,  $h$  is Planck's constant,  $\nu$  is the photon's frequency,  $E_g$  is bandgap, and  $B$  is a constant. The exponent  $\gamma$  depends on the nature of the electronic transition and is equal to 0.5 for direct and 2 for indirect transition.<sup>[34,35]</sup> For undoped and doped BFO NPs the direct transition has been considered.

For the reflectance spectra the absorption coefficient,  $\alpha$ , can be replaced with the Kubelka–Munk function,  $F(R_\infty)$ . (Where,  $R_\infty$  is the reflectance of the sample)

$$(F(R_\infty)h\nu)^{1/\gamma} = B(h\nu - E_g) \quad (5)$$

We plot corresponding Tauc plots using  $\gamma = 0.5$  (Figure S4, Supporting Information). We observe that there is no large difference between the bandgap of MDT-doped NPs and BFM NPs.

To study the recombination of photoinduced charge carriers we utilized PL spectroscopy. All samples show a broad PL maximum between 500 and 700 nm. However, the PL intensity and the position of the PL maximum change drastically upon doping (Figure 3b,c). BFO NPs have the highest PL intensity. Doping with Mn reduces it by about four times. Further doping with Ca or Dy does not significantly change the PL, but for Ag-BFM the PL intensity reincreases by a factor of 2.5. Interestingly, the Dy-BFM NPs have the lowest PL intensity among all NPs under study.

Upon closer examination, it turns out that the total PL signal is a superposition of two PL peaks at 560–575 and 605–625 nm (Figure S5a–f, Supporting Information). For the BFO NPs, the main peak at  $\approx 562$  nm (2.21 eV) corresponds to emission from the bandgap, and the second (lower) peak at  $\approx 605$  nm (2.05 eV) is due to defect level emission (DLE). Upon doping, a redshift of the peak positions is observed, which can be attributed to an alteration in the electronic energy levels. Since PL emission spectra arise because of radiative recombination of electrons and holes, a smaller area of the emission peak corresponds to a lower recombination rate. The areas of both PL peaks decrease when we dope Mn into BFO (Figure S5f, Supporting Information), whereas the absorption of BFM NPs is higher than that

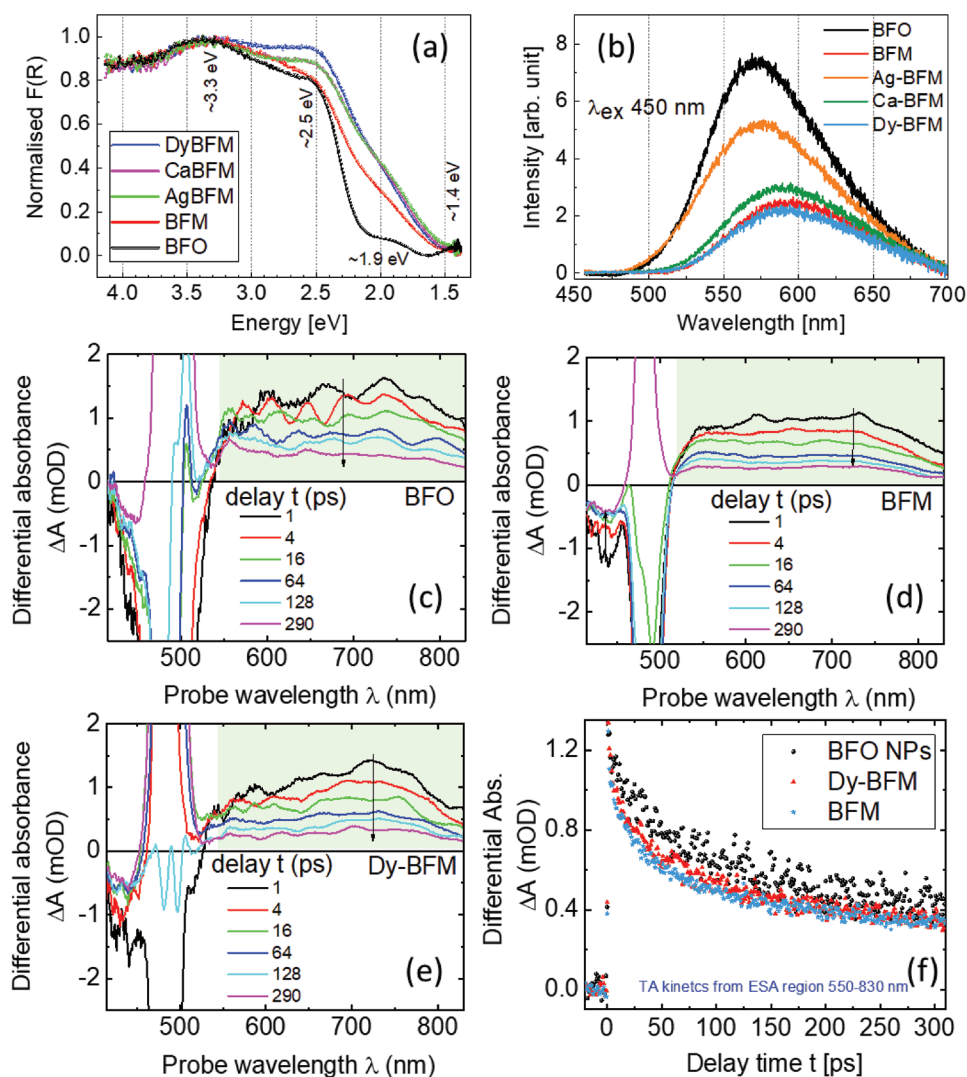


**Figure 3.** Absorbance spectra a), emission spectra b), and transient absorption spectra recorded following 488 nm excitation at various pump–probe delay times for BFO NPs c), BFM NPs d), and Dy-BFM NPs e). f) shows the ESA kinetics with fits, normalized to the BFO kinetics, ascribed to the excited-state evolution (as the bleach stay constant on this time scale).

of BFO NPs (Figure 3a). This means that BFM NPs have a lower recombination rate of photoinduced charge carriers than BFO NPs, which may be associated with doping-induced trap states inside the bandgap. For Ag-BFM NPs, the areas of the PL peaks increase in comparison to BFM. This increase can be due to stronger light absorption by Ag-BFM NPs, as shown in Figure 3. For Ca-BFM NPs, we observed that light absorption is similar as Ag-BFM, but the area of the PL peaks is smaller, which indicates a weaker recombination of the charge carriers than in the case of Ag-BFM NPs. Interestingly, Dy-BFM NPs have the strongest light absorption (Figure 3) but have the smallest PL peak area among all NPs, which indicates the least recombination of charge carriers. In addition, the green peak area corresponding to defect level emission is smallest in the case of Dy-BFM among all. The time resolved photoluminescence decay kinetics of BFO NPs, BFM, and Dy-BFM NPs are shown in Figure S5 (Supporting Information) (red box). The decay kinetics are fitted by a bi-exponential decay function,

$I = A_1 \exp(-t/\tau_1) + A_2 \exp(-t/\tau_2)$ . The average lifetime of charge carriers is calculated using Equation (6)

$$\text{Average } \tau = \frac{[(A_1 \cdot \tau_1^2) + (A_2 \cdot \tau_2^2)]}{[(A_1 \cdot \tau_1) + (A_2 \cdot \tau_2)]} \quad (6)$$

The average lifetime of these NPs is in the range of a few  $\mu\text{s}$  (Table S3, Supporting Information). From the PL emission decay kinetics, the nonradiative average lifetime is lower for BFM than BFO NPs which is due to the presence of trap states. However, for Dy-BFM, the lifetime is larger than BFO NPs, which manifests less recombination of charge carriers. To understand the charge carrier dynamics, especially in Dy-BFM NPs which can absorb most of the light among all NPs, we utilized transient absorption (TA) spectroscopy. In TA measurements, a pump pulse excites the sample and a weak probe pulse delayed by  $\Delta t$  (delay time between pump and probe) analyses

the resulting mixture of ground state absorption (GSA) and excited state absorption (ESA). (Figure S6, Supporting Information) The pump (488 nm, 280 nJ) induced transient absorption signal  $\Delta OD(t, \lambda)$ ; optical density, was measured with a continuum probe in the range of 400–850 nm. The absorption band shows a negative sharp GSA feature between 400 and 530 nm that can be due to bleaching of the ground state,<sup>[36,37]</sup> due to excitation by the higher intensity pump source as shown in Figure 3. Another important feature is the ESA spectrum (green region) in the 550–830 nm range (Figure 3c–f). The ESA spectral intensity decreases with increased delay time due to less population of the excited state. One could trace the light-induced reaction from the photogeneration of charges to their almost disappearance. Comparing the TA spectra of BFO NPs recorded at different pump–probe delay times with BFM and Dy-BFM NPs, a qualitative difference can be observed. For BFM NPs, TA spectral intensities are low compared to BFO NPs at the same delay times which manifests a smaller excited state absorption in BFM than BFO. However, for Dy-BFM NPs the spectral intensity is more than BFM NPs that means a higher number of carriers is available in the excited states than in BFM.

The charge carrier decay dynamics (Figure 3f) of the TA spectra were analyzed at a probe wavelength of 700 nm. The bi-exponential decay fit of the ESA region for the three samples are shown in Figure S7 (Supporting Information). The bleach kinetics in the region of 415–450 nm (Figure S7d, Supporting Information) reveals no change in the long-time behavior unlike the ESA kinetics (Figure S7a–c, Supporting Information). In Figure S7a–c (Supporting Information), the solid lines represent the best fits of the time traces to the sum of the bi-exponential decay function using the following Equation (7)

$$\Delta A(\tau) = A_1 e^{-\tau/\tau_1} + A_2 e^{-\tau/\tau_2} \quad (7)$$

Where, “A” is absorbance, “t” is time, and  $A_1$ ,  $A_2$ , are the pre-exponential factors corresponding to the exponential decays with lifetimes of  $\tau_1$ , and  $\tau_2$ , respectively. From Table S4 (Supporting Information), there are two types of components with shorter and longer decay times. The average lifetime is calculated using Equation (8)

$$\text{Average } \tau = \frac{[(A_1 * \tau_1) + (A_2 * \tau_2)]}{[A_1 + A_2]} \quad (8)$$

BFO NPs possess the longest average lifetime, whereas Dy-BFM possesses the shortest. The shorter decay lifetimes are attributed to the presence of trap-states, which introduce additional pathways for nonradiative recombination of charge carriers.

### 2.3. Photocatalytic Activity of NPs

To study the role of MDT dopants on the photocatalytic (PC) performance of BFM NPs, we carried out experiments on the photodegradation of the organic dye rhodamine B (RhB). According to our previous work, lowering the pH value to 2.2 helps to improve the PC rate by reducing dispersion settling.<sup>[22]</sup>

We also noticed similar results for MDT-doped BFM NPs, where at a pH of 2.2 the PC rate is higher than at pH = 4.4. Figure S8 (Supporting Information) shows the absorption spectra of the RhB dye in the process of photo-stimulated degradation in the presence of various NPs. Figure 5d shows the time required for the total degradation of RhB at pH 2.2 and the corresponding rate constant (Figure 5b). The degradation of the dye in the presence of MDT-doped NPs occurs faster than in the case of BFM or BFO NPs. The order of the rates for total degradation is: Dy-BFM > Ca-BFM > Ag-BFM > BFM > BFO. Dy-BFM NPs are capable of degrading all dye within 60 min. It should be noted that the observed PC activity of the NPs follows a similar trend as the surface area of the NPs (Figure 8). Therefore, it can be concluded that the degradation rate is strongly influenced by the surface area of NPs, since a large surface provides more reaction sites for photocatalysis. In addition, the total light absorption by Dy-BFM is also the highest among all NPs, which contributes to the creation of the largest number of photoinduced charge carriers.

We also studied photocatalysis assisted by ultrasonication (US) keeping the other conditions as before (pH 2.2, UV-visible light). The absorption spectra of RhB in the presence of US at pH 2.2 are shown in Figure 4. The total degradation trend and the rate constant are shown in Figure 5c,d, respectively. We found that photodegradation of RhB under US conditions occurs faster than under non-US condition. Moreover, the order of the NPs in terms of the photocatalysis effectiveness changes and becomes: Ag-BFM > Dy-BFM > Ca-BFM > BFM ~ BFO. The increase of the PC performance under US conditions indicates that factors other than the surface area or light absorbance may play a role. It has been discussed in the literature that such an enhancement of the photocatalytic activity can be related to the hydrostatic piezoelectric effect and the underlying ferroelectric properties of NPs.<sup>[38]</sup>

### 2.4. Ferroelectricity in MDT Doped BFM NPs

The standard way for measuring ferroelectricity and the piezoelectric effect requires a dense, electroded sample, which cannot be achieved with NPs. Even compacted into pellets, they still have a low density and contain a large volume of voids and pores, which completely distort the internal electric field distribution inaccessible to experiment. It is then difficult to apply a sufficiently strong electric field to the NPs. Extracting information on the polarization and piezoresponse of NPs from the overall response of such nanopowder-air composite is a non-trivial and error-prone task. Therefore, to confirm the ferroelectricity in the NPs under study, we used piezoresponse force microscopy (PFM). PFM has established itself as a reliable method for studying ferroelectric and piezoelectric properties at the nanoscale, even within individual NPs.<sup>[10,39]</sup> The results of PFM measurements of the MDT doped BFM NPs are shown in Figure 6 (PFM images of BFO and BFM particles have been reported elsewhere).<sup>[23]</sup>

Figure 6a,d,g shows the topography of the NPs. It can be seen that the average particle size is smaller than 50 nm. There are large agglomerates of Ag-BFM NPs in contrast to the other studied NPs. Figure 6b,e,h shows the corresponding vertical

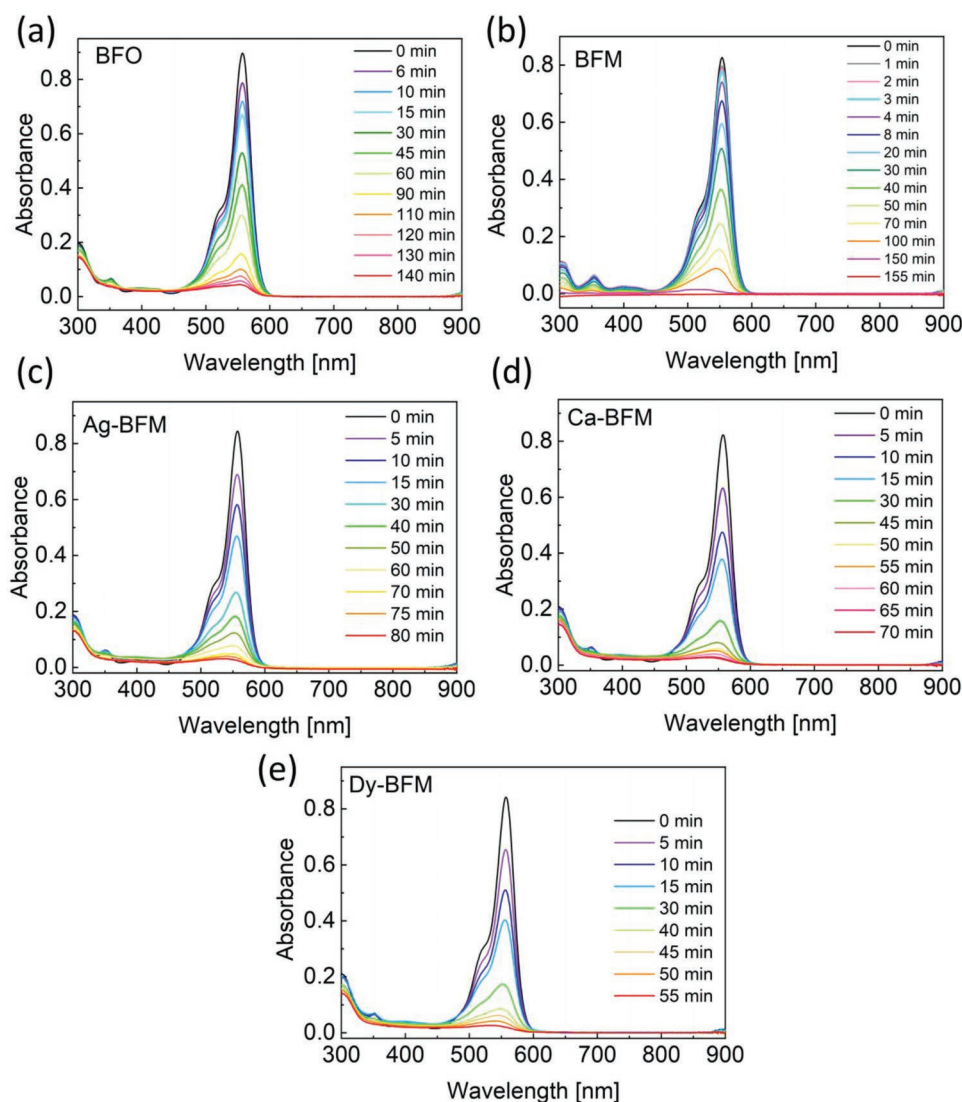


**Figure 4.** Photocatalysis at pH 2.2 and in the presence of ultrasonication (US). The absorption spectra represent the degradation of the Rhodamine B with time for MDT-doped BFO NPs a–e).

PFM (VPFM) amplitude and Figure 6c,f,i represents the VPFM phase images. The VPFM signal corresponds to the longitudinal piezoelectric effect and reflects the distribution of the out of plane polarization component. From the phase images in can be seen that most of the particles are in a single-domain state. In the amplitude images the brighter zones correspond to the NPs with larger piezoresponse. The local piezoresponse hysteresis loops shown in Figure 6k,l,m confirm that the polarization direction in the codoped NPs can be switched by an electric field, i.e., the NPs retain the ferroelectric state. The local hysteresis is most open for Ag-BFM NPs, and least so for Ca-BFM.

At first glance it can be seen that Ca-BFM has a lower piezoresponse than the Ag-BFM and Dy-BFM samples. To quantify the variation of the piezoresponse in respect to the chemical composition, we compare between particles showing the maximum VPFM amplitude signal (Figure 5j). The data for the BFO and BFM samples are taken from our previous publica-

tions,<sup>[23,22]</sup> and the VPFM amplitude is normalized to the probe voltage. Here we have considered that the longitudinal piezoresponse depends on the crystallographic orientation of the particles with respect to the laboratory coordinate system. Therefore, we expect that the NPs showing the maximum VPFM signal will have similar crystallographic orientation. It can be seen that Ag-BFM has the highest piezoresponse, followed by Dy-BFM, whereas Ca-BFM has the smallest piezoresponse among all the samples studied. We observe that doping with Ca reduces the piezoresponse of BFM NPs similar to what was found by substitution of Bi by another divalent cation ( $\text{Ba}^{2+}$ ).<sup>[23]</sup> Since piezoresponse is proportional to the local polarization value, it can be concluded that A-site doping of BFO NPs by divalent elements suppresses the polarization, whereas trivalent ( $\text{Dy}^{3+}$ ) and monovalent ( $\text{Ag}^+$ ) cations provide an increase of polarization.

The observed polarization tendency is related to a doping induced modified crystal structure of the pristine BFO NPs.



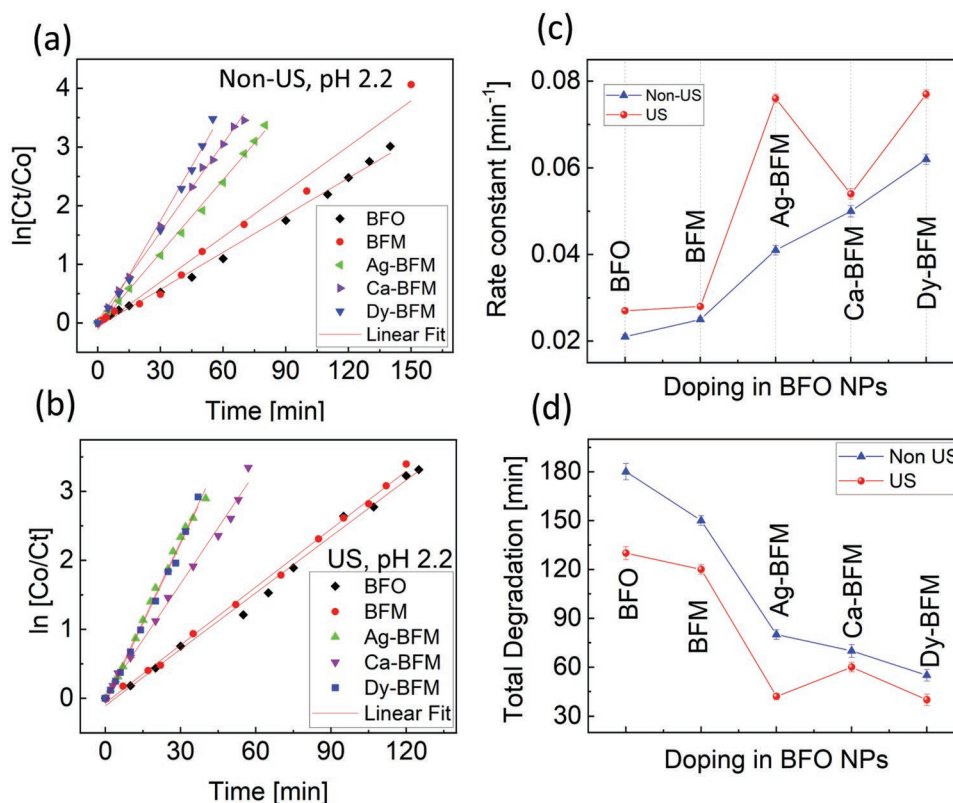


**Figure 5.** Reaction kinetics of photocatalysis in nonultrasonication (non-US), and ultrasonication (US) conditions at pH 2.2 and c,d) shows the rate constant and total degradation time trend, respectively, in both conditions.

Therefore, the structural changes which leads to higher polarization in mono and trivalent cation doped BFM NPs are probed. The off-center displacement of Bi in the rhombohedral ( $R3c$ ) structure of BFO is the main responsible factor for its polarization. Such displacement can be estimated by calculating the Bi–O bond distances of the Bi-distorted cuboctahedron in the  $R3c$  structure formed by the 12 nearest neighboring oxygen atoms (Figure 7). In the distorted cuboctahedron of bulk BFO, six oxygen atoms are in the plane perpendicular to the polar axis  $[111]_c$ , forming a hexagon with Bi at the top of it and off displaced from the center. Three oxygens are in the plane below the hexagon and three oxygens are in the plane above it, forming the triangular base. Based on the Bi–O bond distances, four groups are divided from shortest:  $(1.1)_3$ ,  $(1.2)_3$ ,  $(1.3)_3$ , to longest:  $(1.4)_3$  and are represented in different colors.<sup>[40]</sup>

To investigate the alteration in the Bi–O and Fe–O distances in doped BFO NPs, we measured and analyzed extended X-ray absorption fine structure (EXAFS) spectra of Bi-L<sub>III</sub> edge and Fe-K edge shown in Figure 8a,b. Bi-L<sub>III</sub> near edge spectra consist of two main features B1 and B2, where B1 is the first inflection point of the spectrum and shows the absorption edge energy value corresponding to the  $2p^{3/2} \rightarrow 6d$  transition.<sup>[41]</sup> All spectra correspond to the Bi<sup>3+</sup> state. We observe three features in the Fe-K edge spectra: A1, A2, and A3. The pre-edge A1 feature is attributed to the O-1s to Fe-3d quadrupole forbidden transition, A2 corresponds to the O-2p to Fe-3d ligand to metal transition, and A3 is due to the O-1s to Fe-4p dipole allowed transition.<sup>[41]</sup> The change in intensity shows the alteration in electron density

and hybridization between metal Fe (3d) and ligand O (2p). There is a significant difference in intensity found for absorption edges of Dy-BFM from the others.

After deconvoluting the peaks, we have calculated the Bi–O, Fe–O, Fe–Bi, and Fe–Fe bond distances shown in Figure 8c,d. We found that for BFO NPs, there are two shorter Bi–O, and two longer Bi–O bond distances (Figures 8c, and 7).

From Figure 8c, upon Mn doping into BFO NPs there is not a big change in the four Bi–O distances, except a slight decrease of Bi–O (1.2) and Bi–O (1.3). This shows that doping by Mn does not alter the Bi–O distances significantly so there is no big effect on the polarization of BFO NPs into which Mn is incorporated (Figure 6j). Whereas the Fe–O bond distances in one unit cell, i.e., Fe–O (1.1)<sub>3</sub> and Fe–O (1.2)<sub>3</sub>, decrease and increase, respectively, due to Mn-doping (Figure 8d). This might be one of the major factors influencing the magnetic properties of BFM NPs.<sup>[22,23]</sup>

Upon monovalent Ag doping into BFM NPs, the shorter Bi–O distances (Bi–O (1.1)<sub>3</sub> and (1.2)<sub>3</sub>) slightly increase by 1% and 2%. However, the longer Bi–O distances (Bi–O (1.3)<sub>3</sub> and (1.4)<sub>3</sub>) significantly decrease to 19% and 8% to BFM NPs, which alters the distorted-cuboctahedron and corresponds to an increment in polarization. Divalent Ca-doping into BFM NPs, results in a decrement of all four Bi–O bond distances, 3%, 6%, 21%, and 18% from the shortest to the longest, respectively. This makes the distorted cuboctahedron a bit more symmetrical and brings Bi toward the plane of the hexagon, which can explain

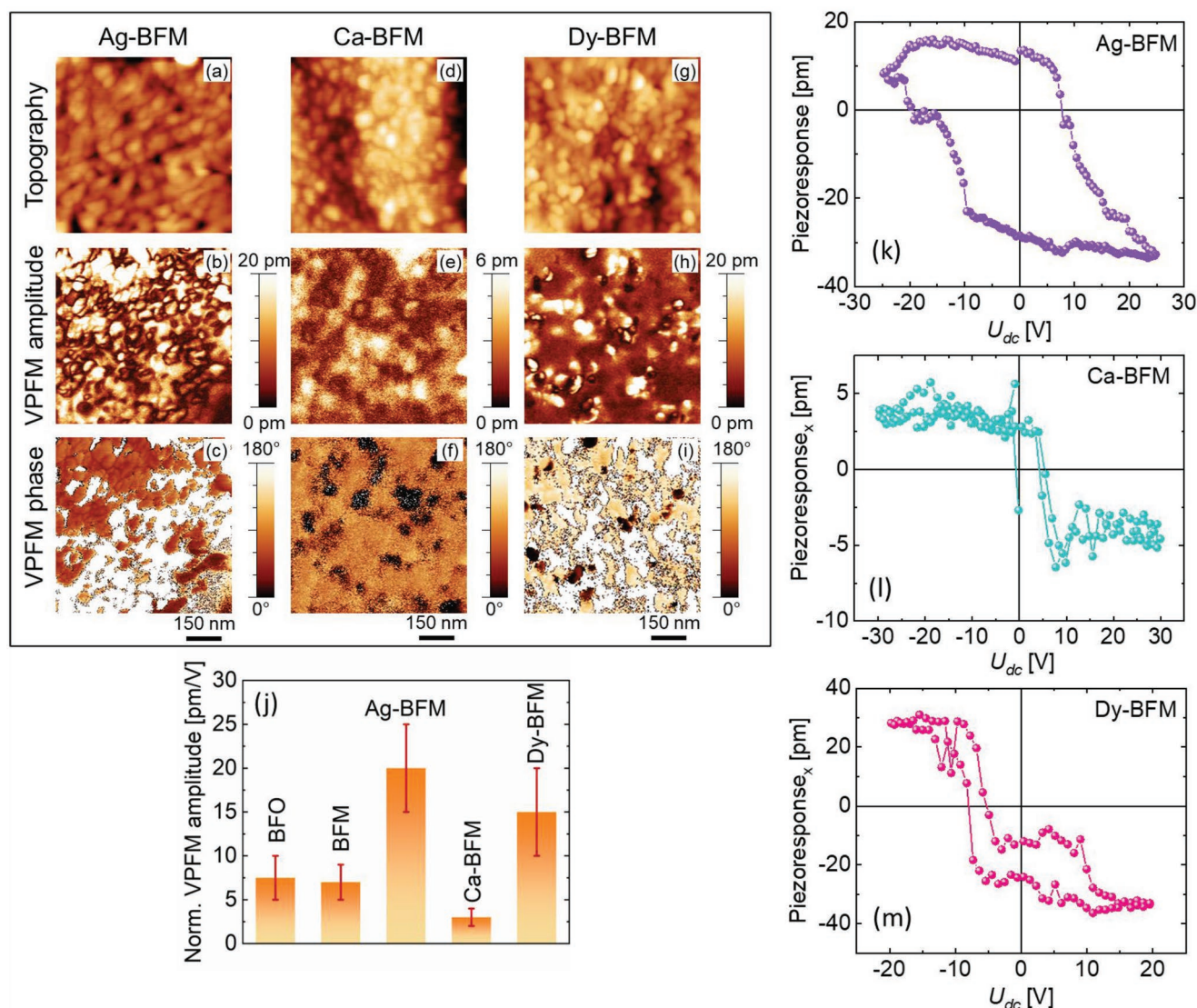


**Figure 6.** Piezoresponse force microscopy (PFM) images for MDT-doped BFO NPs in black box a–i). Topmost pictures represent topography. The middle ones show the normalized vertical PFM amplitude. The lowest row of images are vertical phase images. Comparison of VPFM amplitude j). Hysteresis loops k–m) for MDT-doped BFO NPs, respectively.

the lower polarization for divalent cation doped BFM NPs. Similar results are also observed by us for Ba-doped BFM NPs. For trivalent Dy-doped BFM NPs, the bond distances change similar to the monovalent case, however, here is a slight decrement of 0.5% for Bi–O (1.1)<sub>3</sub>, an increment of 2% for Bi–O (1.2)<sub>3</sub>, and again decrements of 17% and 7% for Bi–O (1.3)<sub>3</sub> and Bi–O (1.4)<sub>3</sub> bonds, respectively.

Such changes in the crystal structure via alterations in the Bi–O distances may lead to higher polarization and piezoresponse in Ag-BFM NPs and Dy-BFM NPs and lower polarization in Ca-BFM NPs. The changes in the Fe–O bond distances are relative changes. They are important to explain the change in magnetic properties of MDT-doped BFM NPs and will be discussed elsewhere. Our results show that divalent cations affect the crystal symmetry in a different way than monovalent and trivalent cations do. That is how different

types of dopants can be chosen for increasing or decreasing the polarization.

### 3. Discussion

#### 3.1. Photocatalytic Mechanism

During photocatalysis, the charge carriers (electrons:  $e^-$  and holes:  $h^+$ ) are generated upon light absorption by the NPs. Without recombination these charge carriers should migrate from the bulk to the particle's surface, where they produce active species: the oxygen radical,  $O_2^{\cdot-}$ , and the hydroxide radical,  $OH^{\cdot}$ , from water. These active species then further react with the RhB dye present in the water degrading it into  $CO_2$  and  $H_2O$ . The production of a large number of active radicals

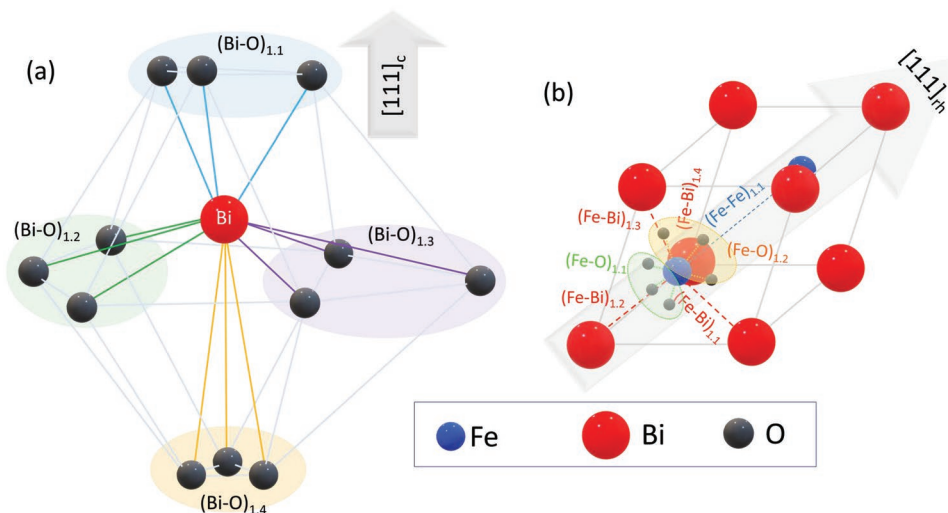


**Figure 7.** Bi-cuboctahedron schematic in rhombohedral BiFeO<sub>3</sub> NPs, where four groups of oxygens atoms are being represented in different colors based on Bi–O bond distances a). Schematic of Fe–O, Fe–Bi, and Fe–Fe bond distances in the unit cell of BiFeO<sub>3</sub>.

is vital for fast photocatalytic activity. The generation of O<sub>2</sub> and OH<sup>•</sup> happens at certain energy balance conditions, as shown in **Figure 9**. To form these active species the conduction band (CB) and valence band (VB) of the photocatalyst must be levelled to transfer the charge carriers *e*<sup>−</sup> and *h*<sup>+</sup> into the water and enable the water splitting. Therefore, we need to estimate the positions of the CB and the VB for the NPs. The positions of VB maxima can be obtained from Ultraviolet Photoelectron Spectroscopy (UPS) data (Figure S9, Supporting Information). Adding the bandgap (*E<sub>g</sub>*) width available from the DRS results (Figure S4, Supporting Information), we can predict the positions of the CB minima as shown in Figure 9. According to the energy levels diagram in Figure 9, we can conclude that the BFO NPs are not able to produce the O<sub>2</sub> radicals since the electrons cannot be transferred. Nevertheless, to produce the OH<sup>•</sup> radicals the VB edge suits quite well. So, BFO NPs mainly produce OH<sup>•</sup> radical to degrade RhB. From the estimated CB edge value of BFO, it should be able to produce hydrogen [H<sup>+</sup>/H<sub>2</sub>: 0 eV] via water splitting. For BFM NPs, the positions of the CB and VB edges are similar to those in BFO. Therefore, it can be assumed that both types of NPs are sources of the formation of OH<sup>•</sup> radicals. For Ag-BFM NPs, the CB edge is lower than energy level of O<sub>2</sub>/O<sub>2</sub><sup>•−</sup> so they cannot produce O<sub>2</sub>. However, OH<sup>•</sup> radicals can be produced easily. Hence OH<sup>•</sup> radicals are responsible for photocatalysis on Ag-BFM NPs similar to BFO NPs. Whereas, in the case of Ca-BFM and Dy-BFM O<sub>2</sub> radicals are easily produced as per positions of their CB and VB levels. The undoped BFO, BFM, and monovalent doped BFM NPs produce OH<sup>•</sup> radicals to degrade RhB dye, but di-, and tri-valent doped BFM NPs generate O<sub>2</sub> radicals to accomplish the RhB degradation.

Several factors jointly play a role in determining the final photocatalytic activity of doped BFO NPs. The smaller size of the NPs leads to an advantageously large surface area and therefore, a large number of active sites per volume of photocatalyst becomes available to promote PC. **Figure 10** demonstrates the correlation between the surface area and the time required for complete photodegradation of the RhB dye for the NPs under study.

The ferroelectric nature of the NPs is believed to be beneficial for photocatalytic activity.<sup>[8,21]</sup> The mechanism is not entirely clear yet, but it is assumed that the spontaneous polarization results in a depolarization electric field, which promotes the separation of photoinduced charge carriers.

### 3.2. Photocatalytic Mechanism in an Ultrasonication (US) Environment

Ultrasonic treatment has been widely used to drive chemical reactions.<sup>[42]</sup> Ultrasonication generates alternating low-pressure and high-pressure waves in liquids, leading to the formation and violent collapse in very short times (a few microseconds) of small bubbles. This phenomenon is termed into cavitation and causes high-speed impinging liquid jets and strong hydrodynamic shear-forces. The cavitation bubble collapses near or at the surface of particles with lots of energy. This generates shock waves, which are usually used to remove contaminants from the surface of the particles. When the bubbles collapse, local pressure of the order of 135 MPa can be reached.<sup>[43,44]</sup> This effect is also used to deagglomerate nanometer-size materials. Though the pressure provided by ultrasonicator (135 MPa) is not enough to distort the pristine crystal structure (rhombohedral; R3c) of BFO,<sup>[45]</sup> ultrasonication (480 W, 40 kHz) can induce a piezoelectric effect in presence of light irradiation. When a ferroelectric material, like MDT doped-BFO NPs, experiences a hydrostatic stress, the induced displacement of ions causes an alteration in the polarization resulting in a release of the screening charges that can participate in the catalysis (**Figure 11**).

The hydrostatic piezoelectric effect induces a change of the polarization  $\Delta P = -p(2d_{31} + d_{33})$ . Taking the piezoelectric coefficient for bulk BFO  $d_{31} = -4.5$  pC/N and  $d_{33} = 18$  pC/N,<sup>[46,47]</sup> one can estimate that a pressure of 135 MPa acting on a NP upon ultrasonication decreases its polarization by  $\Delta P = 0.12$   $\mu\text{C cm}^{-2}$ . This will lead to an excess of free charge carriers near to the surface of NPs. Before the hydrostatic stress

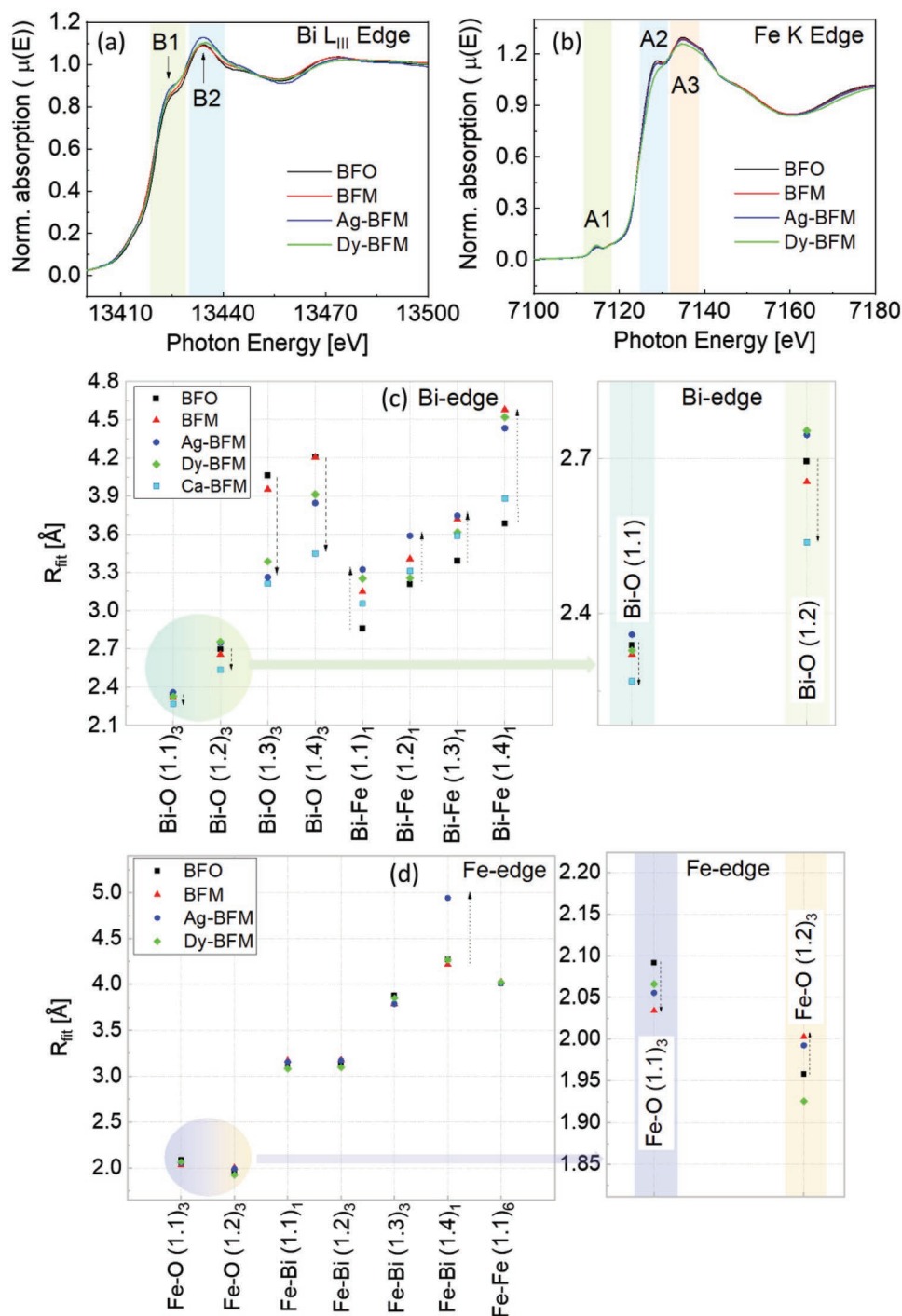


**Figure 8.** XAFS spectra of Ag, Ba, Dy, and Mn codoped and undoped BiFeO<sub>3</sub> NPs: Bi L<sub>III</sub>-absorption edges a) and Fe K-absorption edges b), Fitted bond distances (follow Figure 7) from Bi-edge c), and from Fe-edge d), respectively, for all NPs. Subscript represents the coordination number of Bi and Fe.

is removed, and before this excess charge is compensated by external screening (H<sup>+</sup> and OH<sup>-</sup> ions in solution), it can be used for a redox reaction to degrade the dye. The efficiency of such a mechanism of piezocatalysis depends on the balance between the rate of the redox reaction of charge carriers with adsorbed species, the external and internal screening rate, and the pressure release time.

In our understanding, the enhancement of the PC effectiveness under US treatment could be caused by three major factors. First, ultrasonic treatment provides a more efficient interaction of dye molecules with the surface of nanoparticles due to intensive mixing. Second, it breaks NPs agglomerates and increases the active surface area. Third, ultrasonication induces hydrostatic piezoelectric effect increasing density of

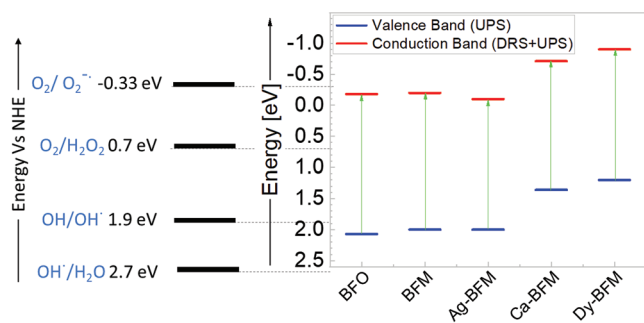


**Figure 9.** Schematic of the energy levels of the active species during photocatalysis. The right graph shows the calculated valence band level from UPS data and the estimated conduction band edge with the help of the bandgap calculation from the DRS of the NPs.

charges that can participate in redox reactions.<sup>[48]</sup> Despite the fact that Ag-BFM NPs have a smaller surface area and exhibit lower light absorption and stronger recombination of photo-induced charge carriers, which is confirmed by the PL spectra, than Dy-BFM NPs, they show better PC performance under ultrasonic conditions (Figure 5c, Supporting Information). This can be explained by a stronger effect of the third factor. Indeed, the Ag-BFM NPs have a greater piezoresponse than the Dy-BFM ones, and, consequently, the hydrostatic piezoeffect will generate more surface charges for reactions with dye molecules, which will lead to a faster decrease in the concentration of the latter.

#### 4. Conclusion

We have compared the effect of the mono-, di-, and tri-valent cation doping at the Bi-site on the photocatalytic efficiency and ferroelectric properties of Mn-doped BFO NPs. Monovalent doped Ag-BFM NPs and trivalent doped Dy-BFM NPs have increased polarization in comparison to both pristine and Mn-doped BFO NPs, due to favorable distortion of their crystal structure, confirmed from EXAFS data. On the contrary, divalent Ca doping weakens the ferroelectric properties in the same way as was shown for doping with Ba.

We studied the photocatalytic efficiency of MDT doped BFO NPs via mineralization of the RhB dye. We found that under normal conditions, Dy-BFM NPs exhibit the highest photocatalytic activity due to the largest surface area, the highest light absorption coefficient, the slowest recombination of photoinduced charge carriers, and a large polarization. Most of the nanoparticles are single domain ferroelectrics, where the spontaneous polarization creates an internal depolarization field. Though this field can be screened, but even a partially screened depolarization field can be a driving force for the photo-induced charge carrier separation in such single domain FE photocatalysts. The importance of the large polarization and related piezoresponse becomes obvious for ultrasound assisted photocatalytic degradation of the dye. In this case, a significant improvement of the photocatalytic activity was observed for the Ag-BFM NPs, which have the largest polarization among the measured compositions. Piezoresponse (polarization) becomes

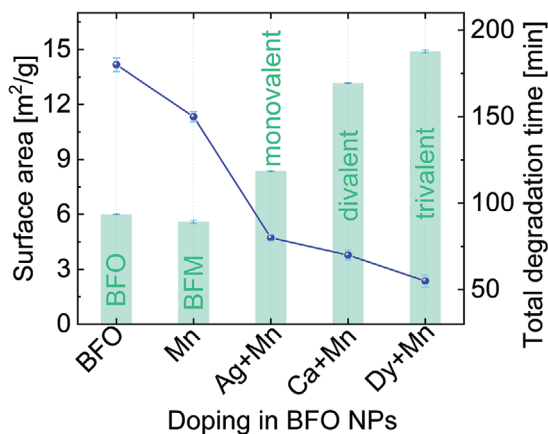


**Figure 10.** Total photodegradation time of Rhodamine B dye without ultrasonication and surface area with respect to doping in BFO NPs.

especially important factor under ultrasonic conditions for ferroelectric photocatalysts.

The obtained results clearly show that the spontaneous polarization and piezoelectric effect substantially affect the photocatalytic properties of the nanoparticles. Therefore, development of narrow bandgap ferroelectric NPs with a large hydrostatic piezoelectric coefficient is promising to achieve better photocatalytic efficiency.

#### 5. Experimental Section

MDT and Mn codoped BFO NPs ( $\text{Bi}_{0.95}\text{A}_{0.05}\text{Fe}_{0.95}\text{Mn}_{0.05}\text{O}_3$ ; A = Ag, Ca, Dy) were synthesized by a modified wet chemical “sol–gel route” followed by a calcination step at 773 K.<sup>[23]</sup> Bismuth nitrate  $\text{Bi}(\text{NO}_3)_3 \cdot 5\text{H}_2\text{O}$  ( $\geq 98\%$ ), Iron nitrate  $\text{Fe}(\text{NO}_3)_3 \cdot 9\text{H}_2\text{O}$  ( $\geq 98\%$ ), Manganese acetate  $\text{Mn}(\text{CH}_3\text{COO})_2 \cdot 4\text{H}_2\text{O}$  ( $\geq 99\%$ ), Calcium nitrate  $\text{Ca}(\text{NO}_3)_2 \cdot 4\text{H}_2\text{O}$  ( $\geq 99\%$ ), Silver nitrate  $\text{Ag}(\text{NO}_3)_3$  ( $\geq 99\%$ ), Dysprosium nitrate  $\text{Dy}(\text{NO}_3)_3 \cdot x\text{H}_2\text{O}$  (99.9%), Tartaric acid  $\text{C}_4\text{H}_6\text{O}_6$  ( $\geq 99\%$ ), and Nitric acid  $\text{HNO}_3$  (65%) were purchased from Sigma-Aldrich.

**PC Procedure:**  $10^{-5}$  M of methyl orange (MO) and rhodamine B (RhB) aqueous suspensions were prepared for their photodegradation. To establish an adsorption–desorption equilibrium between the dye and the photocatalyst, 50 mL of organic dye with 0.025 g of NPs were placed into a jacketed beaker in the dark for 30 min. For a well dispersed dye solution, 9 min ultrasonication was applied in the dark. Dye degradation was carried out under the irradiation of a halogen lamp (250–850 nm, LOT-Oriel) in a dark chamber. During PC experiments, continuous magnetic stirring of the NPs was performed to avoid their settling. For the PC in an acidic medium, the pH of the dispersion (dye + NPs) was adjusted to 2.2 by adding a few drops of 2N  $\text{HNO}_3$ . To keep a constant temperature (298 K) during PC and avoid thermal catalytic effects, a continuous water flow was maintained around the jacketed beaker. To study the degradation of the dye, 1 mL solution was taken every 5 min and centrifuged using a Hettich Zentrifugen Universal 320 R centrifuge at 9000 RPM for 10 min in the dark to separate the NPs. Afterward, absorption measurements were performed on the centrifuged solutions. After the complete degradation of the dye (colorless solution), the NPs were conveniently separated with the help of magnets under the PC vessel and used for the next cycles of PC. The stability was checked of NPs after Photocatalytic reaction, using XRD and TEM and found that NPs can be used for at least three next PC cycles.

**US Conditions:** An ultrasonicator of 480 W, 40 kHz (Palssonic, Allpax Germany) was used for performing PC under ultrasonic excitation. All the other conditions were kept as before.

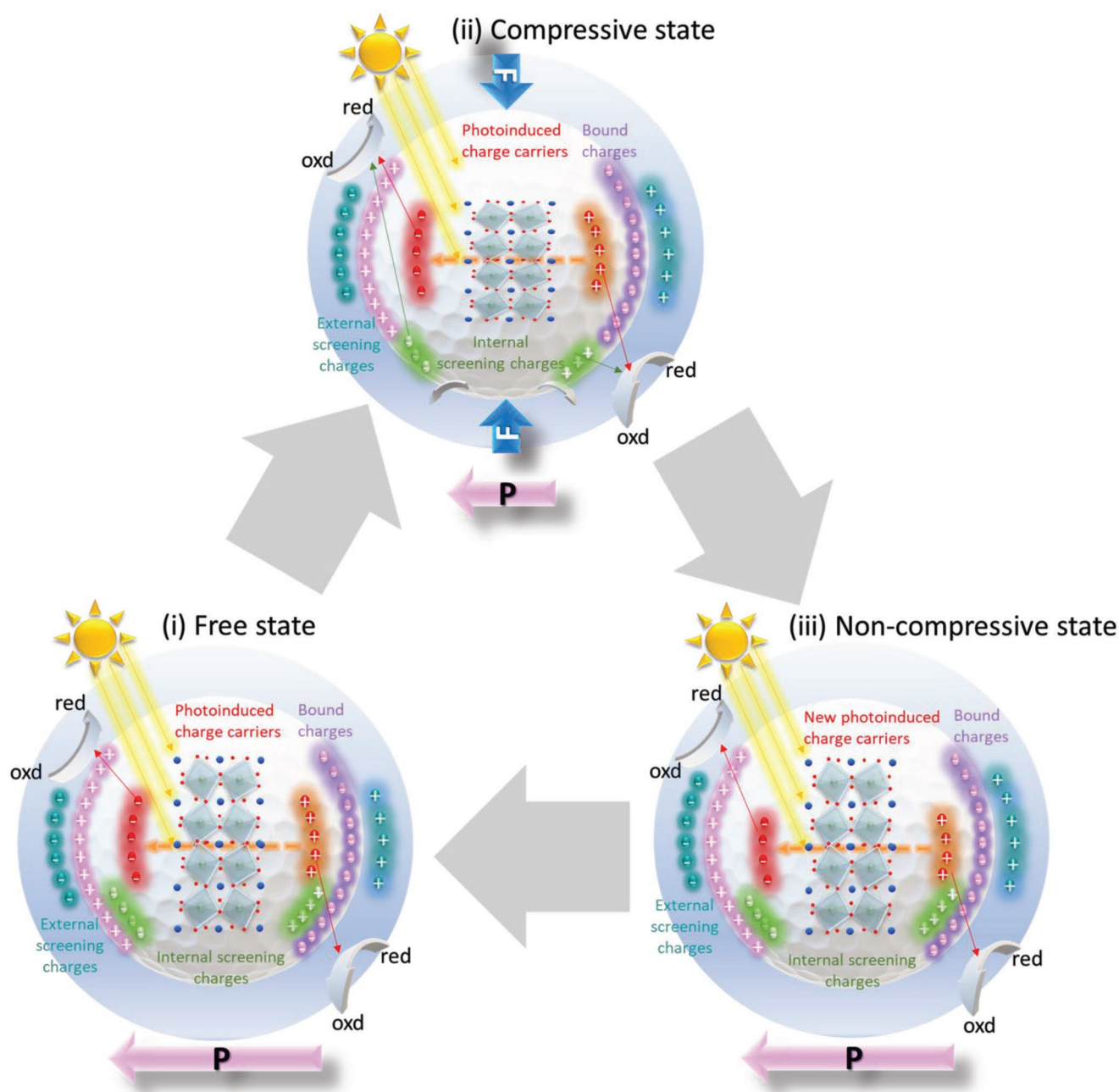


**Figure 11.** Schematic for the role of screening charges in piezo-photocatalysis depending upon the change of polarization (as per material's piezoelectric coefficients) by applied external stress.

**XRD:** The crystalline phase and lattice parameters of all NPs were studied by powder XRD using a Panalytical Empyrean (Cu  $K\alpha$  radiation) diffractometer over a 2-theta range of  $10^\circ$ – $80^\circ$  with a step size of  $0.026^\circ$ . For measurement, the powders were placed on a standard sample holder as a thin flat layer and measured in reflection mode (Bragg–Brentano geometry). The background parameters, zero shift and detector shifts, lattice parameters, and atomic coordinates for the host and the doping atoms, profile parameters (Pseudo-Voigt function including crystallite size, and strain parameters) were fitted simultaneously using the Rietveld refinement procedure realized in the High Score Plus software.

**TEM:** The size and crystallinity of the NPs were analyzed by high-resolution TEM on a JEOL JEM-2200FS microscope using 200 kV acceleration voltage and a probe side aberration corrector. The atomic

composition of the NPs was estimated by energy dispersive X-ray spectroscopy (EDXS) and HAADF using an analytical SEM device (EDS, energy resolution  $< 132$  eV for Mn  $K\alpha$ , detector area  $10$  mm $^2$ ).

**Nitrogen Physisorption Measurements:** The specific surface area of the NPs was determined from nitrogen sorption measurements using a Coulter SA 3100 analyzer (Beckman Coulter). The samples were degassed under vacuum at room temperature for 24 h. The Brunauer–Emmett–Teller (BET) equation was applied to determine the specific surface areas of the NPs. The Barrett–Joyner–Halenda (BJH) method was applied to determine the pore volume distribution.

**PFM:** To address the ferroelectric properties of the NPs, PFM measurements were performed using a commercial scanning probe microscope MFP-3D (Asylum Research). Pt/Cr coated cantilevers Multi

75E-G (Budget Sensors) with a spring constant of  $3 \text{ N m}^{-1}$  were used. PFM measurements were conducted at a probing voltage amplitude of  $U_{ac} = 5 \text{ V}$  and a frequency  $f = 50 \text{ kHz}$ . The NPs were drop-casted onto a conductive carbon tape for the PFM measurements. The drop-casted NPs were dried in a desiccator over night before PFM measurements.

**UV-Vis Spectrometry:** Diffuse reflectance spectra (DRS) of the NPs were collected using a UV-Vis spectrometer Shimadzu 2600 in the wavelength range 300–900 nm. The NP-powder was pressed and then measured inside an integrating sphere in reflectance mode. Barium sulfate was used as a reference and the baseline was corrected before recording each spectrum. Transmission spectra of diluted NPs and NPs drop-cast onto quartz substrates were recorded using a Shimadzu UV-2550 spectrometer equipped with an integrating sphere in transmission geometry.

**Photoluminescence and Time-Resolved Photoluminescence Spectrometry:** Time-resolved spectra were recorded with a Hamamatsu C5680 streak camera system operated in single-sweep mode using a delay generator with the D-C-450 laser diode in external triggering mode for long time ranges. For shorter times, the same camera was operated in synchroscan mode with a frequency-doubled Coherent Mira Optima 900 Ti: Sa laser in fs operation at 450 nm. All spectra were corrected by the instrument response function and transformed into the energy regime applying the Jacobian conversion.

**Transient Absorption (TA) Measurements:** The TA setup and the method have been described elsewhere.<sup>[36,37,49,50]</sup> Briefly, TA spectra are recorded with 16 forward and backward pump-probe scans, with 1 ps steps. The TA signal consists of three contributions: negative bleach, negative stimulated emission (SE), and positive excited-state absorption (ESA). The spectra are measured at a pump energy of 280 nj. Here, a negative bleach signal can be traced from 415 to 450 nm (before the scattering starts) while ESA extends from 550 to 830 nm. Band integrals taken over these regions give accordingly give the ground-state recovery (not happens) and the excited-state evolution.

**Emission Spectrometry:** To measure the emission spectra, a Varian Cary Eclipse Fluorescence spectrophotometer was used. A 450 nm laser excitation source was used to collect emission spectra in the range from 550 to 650 nm. A stable dispersion of NPs was prepared in ethanol (optical grade) and a baseline was obtained by measuring pure ethanol. The samples were dissolved in optical grade ethanol and treated in an ultrasonic bath for 10 min. The concentration of all types of NPs were kept the same during the PL measurements.

**EXAFS:** EXAFS spectra for Bi  $L_{III}$  absorption edges (13.4186 keV) were recorded in transmission at the BAMline at the Helmholtz-Zentrum Berlin (BESSY II, Berlin, Germany)<sup>[51]</sup> with horizontally polarized hard X-rays from a 7 T shifter at room temperature in air. The signal from the upstream ionization chamber is filled with xenon for the normalization of the X-ray incoming intensity. Powders were mixed with hexagonal BN powder to get correct transmission and pressed between 50  $\mu\text{m}$  thick Kapton foils in pellets of 1 mm thick for the measurement. As reference, X-ray absorption spectra of pure Bi foil was recorded at the same absorption edge.

EXAFS spectra at the Fe and Mn K-edges (7.1120 and 6.5390 keV, respectively) were recorded in the fluorescence mode (TFY) at the same beamline. Four-element energy dispersive detector was used to collect the fluorescence signal in a similar way as in.<sup>[52]</sup> As references, X-ray absorption spectra of pure Fe and Mn foils were recorded at the same absorption edges by TFY.

Typically, for each sample and each absorption edge, 2–3 measurements were performed and further averaged to improve statistics. Data evaluation, analysis, and simulation have been performed using the IFEFFIT software.<sup>[53,54]</sup>

**UPS:** XPS and UPS measurements were performed on a VersaProbe II System by UlvacPhi. For XPS, a monochromatized Ag-K $\alpha$  source with a beam diameter of 100  $\mu\text{m}$  was used. For UPS, He I light at 21.22 eV from a He discharge source was used. To measure the HBEC, a negative voltage was applied to overcome the work-function of the analyzer. The NPs were drop-casted onto a conductive Si-wafer for the measurements. For data analysis, a Shirley background was used. The precise way of

fitting depends on the element that is being fitted. In the case of carbon, a Gaussian–Lorentzian curve is representative for one specific species (the same goes for oxygen and silicon).

## Supporting Information

Supporting Information is available from the Wiley Online Library or from the author.

## Acknowledgements

The authors are grateful to DFG (Deutsche Forschungsgemeinschaft) for financial support through the project LU 729/21-1 (Project No. 396469149). They also thank the Helmholtz-Zentrum Berlin für Materialien und Energie for the allocation of synchrotron radiation beamtime. EXAFS measurements were carried out at the BAM-line at the BESSY II electron storage ring operated by the Helmholtz-Zentrum Berlin für Materialien und Energie. They are thankful to Dr. Markus Heidelmann for TEM measurements. The authors thank to Mrs. Claudia Schenk for the BET measurements.

Open access funding enabled and organized by Projekt DEAL.

## Conflict of Interest

The authors declare no conflict of interest.

## Author Contributions

Conceptualization: A.D., Synthesis and characterizations: A.D. Photocatalytic Experiments: A.D. and C.H.K. Data interpretation: A.D. Main draft preparation: AD. PFM analysis: V.V.S. and A.D. EXAFS analysis: K.Y., A.G.B., Editing: A.D., M.E.C., and A.D. Resources: D.C.L. and J.S. Scientific Discussion and interpretation: D.C.L., V.V.S., and A.D.

## Data Availability Statement

The data that support the findings of this study are available from the corresponding author upon reasonable request.

## Keywords

bismuth ferrite, ferroelectric, nanoparticles, photocatalysis, piezoresponse, polarization

Received: June 22, 2022  
Revised: July 26, 2022  
Published online: August 19, 2022

- [1] C. Paillard, X. Bai, I. C. Infante, M. Guennou, G. Geneste, M. Alexe, J. Kreisel, B. Dkhil, *Adv. Mater.* **2016**, *28*, 5153.
- [2] F. Chen, H. Huang, L. Guo, Y. Zhang, T. Ma, *Angew. Chem., Int. Ed.* **2019**, *58*, 10061.
- [3] Y. Li, J. Li, W. Yang, X. Wang, *Nanoscale Horiz.* **2020**, *5*, 1174.
- [4] Y. Wang, M. Zhang, J. Liu, H. Zhang, F. Li, C. W. Tseng, B. Yang, G. Smith, J. Zhai, Z. Zhang, S. Dunn, H. Yan, *Adv. Energy Mater.* **2020**, *10*, 2001802.

- [5] W. Wang, B. Huang, X. Ma, Z. Wang, X. Qin, X. Zhang, Y. Dai, M. H. Whangbo, *Chem. – Eur. J.* **2013**, *19*, 14777.
- [6] Y. Cui, J. Briscoe, S. Dunn, *Chem. Mater.* **2013**, *25*, 4215.
- [7] T. Zhang, W. Lei, P. Liu, J. A. Rodriguez, J. Yu, Y. Qi, G. Liu, M. Liu, *Chem. Sci.* **2015**, *6*, 4118.
- [8] L. Li, P. A. Salvador, G. S. Rohrer, *Nanoscale* **2014**, *6*, 24.
- [9] Y. Liu, S. Ye, H. Xie, J. Zhu, Q. Shi, N. Ta, R. Chen, Y. Gao, H. An, W. Nie, H. Jing, F. Fan, C. Li, *Adv. Mater.* **2020**, *32*, 1906513.
- [10] S. V. Kalinin, D. A. Bonnell, T. Alvarez, X. Lei, Z. Hu, J. H. Ferris, Q. Zhang, S. Dunn, *Nano Lett.* **2002**, *2*, 589.
- [11] A. Bhardwaj, N. V. Burbure, G. S. Rohrer, *J. Am. Ceram. Soc.* **2010**, *93*, 4129.
- [12] L. M. Peter, in *Photocatalysis: Fundamentals and Perspectives*, **2016**, pp. 1–28.
- [13] P. Raizada, V. Soni, A. Kumar, P. Singh, A. A. Parwaz Khan, A. M. Asiri, V. K. Thakur, V. H. Nguyen, *J. Materiomics* **2021**, *7*, 388.
- [14] S. J. Clark, J. Robertson, *Appl. Phys. Lett.* **2007**, *90*, 132903.
- [15] V. V. Shvartsman, W. Kleemann, R. Haumont, J. Kreisel, *Appl. Phys. Lett.* **2007**, *90*, 17.
- [16] D. Lebeugle, D. Colson, A. Forget, M. Viret, *Appl. Phys. Lett.* **2007**, *91*, 10.
- [17] A. M. Kadomtseva, Y. F. Popov, A. P. Pyatakov, G. P. Vorob'Ev, A. K. Zvezdin, D. Viehland, *Phase Transitions* **2006**, *79*, 1019.
- [18] I. Calisir, A. A. Amirov, A. K. Kleppe, D. A. Hall, *J. Mater. Chem. A* **2018**, *6*, 5378.
- [19] X. Bai, J. Wei, B. Tian, Y. Liu, T. Reiss, N. Guiblin, P. Gemeiner, B. Dkhil, *J. Phys. Chem. C* **2016**, *120*, 3595.
- [20] S. Chauhan, M. Kumar, S. Chhoker, S. C. Kalyal, H. Singh, M. Jewariya, K. L. M. Yadav, *Solid State Commun.* **2012**, *152*, 525.
- [21] K. Sarkar, S. Mukherjee, S. Mukherjee, M. K. S. Mitra, *J. Inst. Eng. Ser. D* **2014**, *95*, 135.
- [22] A. Dubey, A. Schmitz, V. V. Shvartsman, G. Bacher, D. C. Lupascu, M. E. Castillo, *Nanoscale Adv.* **2021**, *3*, 5830.
- [23] A. Dubey, M. Escobar Castillo, J. Landers, S. Salamon, H. Wende, U. Hagemann, P. Gemeiner, B. Dkhil, V. V. Shvartsman, D. C. Lupascu, *J. Phys. Chem. C* **2020**, *124*, 22266.
- [24] A. Dubey, M. E. Castillo, V. V. Shvartsman, D. C. Lupascu, S. Salamon, H. Wende, in *2019 IEEE International Symposium on Applications of Ferroelectrics (ISAF)*, IEEE, Piscataway, NJ **2019**, *1*, <https://doi.org/10.1109/ISAF43169.2019.9034963>.
- [25] S. M. Selbach, T. Tybell, M. Einarsrud, T. Grande, *Chem. Mater.* **2007**, *19*, 6478.
- [26] Y. Feng, H. Wang, Y. Shen, Y. Lin, C. Nan, *Mod. Res. Catal.* **2013**, *2*, 1.
- [27] W. Ramadan, P. A. Shaikh, S. Ebrahim, A. Ramadan, B. Hannoyer, S. Jouen, X. Sauvage, S. Ogale, *J. Nanoparticle Res.* **2013**, *15*, 1848.
- [28] P. Chandra Sati, M. Arora, S. Chauhan, M. Kumar, S. Chhoker, *J. Phys. Chem. Solids* **2014**, *75*, 105.
- [29] M. Sakar, S. Balakumar, P. Saravanan, S. Bharathkumar, *Nanoscale* **2015**, *7*, 10667.
- [30] R. D. Shannon, *Acta Crystallogr., Sect. A: Found. Crystallogr.* **1976**, *32*, 751.
- [31] D. Barreca, A. Gasparotto, A. Milanov, E. Tondello, A. Devi, R. A. Fischer, *Surf. Sci. Spectra* **2007**, *14*, 52.
- [32] N. J. Firet, M. A. Blommaert, T. Burdyny, A. Venugopal, D. Bohra, A. Longo, W. A. Smith, *J. Mater. Chem. A* **2019**, *7*, 2597.
- [33] P. Kubelka, F. Munk, *J. Tech. Phys.* **1931**, *12*, 593.
- [34] R. J. Tauc, A. V. Grigorovici, *Phys. Status Solidi* **1966**, *15*, 567.
- [35] J. I. Pankove, *Optical Processes in Semiconductors*, Dover, New York **1975**.
- [36] S. A. Kovalenko, A. L. Dobryakov, J. Ruthmann, N. P. Ernsting, *Phys. Rev. A: At., Mol., Opt. Phys.* **1999**, *59*, 2369.
- [37] S. A. Kovalenko, R. Schanz, H. Hennig, N. P. Ernsting, *J. Chem. Phys.* **2001**, *115*, 3256.
- [38] J. W. F. Woo, *Phys. Rev. B* **1971**, *4*, 1218.
- [39] M. E. Castillo, V. V. Shvartsman, D. Gobeljic, Y. Gao, J. Landers, H. Wende, D. C. Lupascu, *Nanotechnology* **2013**, *24*, 355701.
- [40] I. Laraib, M. A. Carneiro, A. Janotti, *Phys. Rev. B* **2021**, *104*, 035159.
- [41] T. Gholam, A. Ablat, M. Mamat, R. Wu, A. Aimidula, M. A. Bake, L. Zheng, J. Wang, H. Qian, R. Wu, K. Ibrahim, *Phys. Lett. A* **2017**, *381*, 2367.
- [42] H. M. Santos, C. Lodeiro, J. L. Capelo-Martínez, in *Ultrasound in Chemistry: Analytical Applications* (Eds: J. L. Capelo-Martínez), **2008**, Ch. 1.
- [43] L. Azar, *Control. Environ.* **2009**, *14*, <http://www.absotecthailand.com/docs/Cavitation.pdf>.
- [44] A. Henglein, M. Gutiérrez, *J. Phys. Chem.* **1993**, *97*, 158.
- [45] R. Chandiramouli, V. Nagarajan, *Process. Appl. Ceram.* **2017**, *11*, 120.
- [46] M. Graf, M. Seplarsky, R. Machado, M. G. Stachiotti, *Solid State Commun.* **2015**, *218*, 10.
- [47] G. Jian, F. Xue, Y. Guo, C. Yan, *Materials* **2018**, *11*, 2441.
- [48] F. Mushtaq, X. Chen, M. Hoop, H. Torlakcik, E. Pellicer, J. Sort, C. Gattinoni, B. J. Nelson, S. Pané, *iScience* **2018**, *4*, 236.
- [49] J. Moreno, A. L. Dobryakov, I. N. Ioffe, A. A. Granovsky, S. Hecht, S. A. Kovalenko, *J. Chem. Phys.* **2015**, *143*, 024311.
- [50] I. N. Ioffe, M. Quick, M. T. Quick, A. L. Dobryakov, C. Richter, A. A. Granovsky, F. Berndt, R. Mahrwald, N. P. Ernsting, S. A. Kovalenko, *J. Am. Chem. Soc.* **2017**, *139*, 15265.
- [51] H. Riesemeier, K. Ecker, W. Görner, B. R. Müller, M. Radtke, M. Krumrey, *X-Ray Spectrom.* **2005**, *34*, 160.
- [52] C. Lutz, S. Hampel, X. Ke, S. Beuermann, T. Turek, U. Kunz, A. Guilherme Buzanich, M. Radtke, U. E. A. Fittschen, *J. Power Sources* **2021**, *483*, 229176.
- [53] B. Ravel, M. A. Newville, H. Artemis, *J. Synchrotron Radiat.* **2005**, *12*, 537.
- [54] M. Newville, *J. Synchrotron Radiat.* **2001**, *8*, 322.